EFFECTS OF PENETRATIVE CONVECTION ON SOLAR DYNAMO

Masada, Youhei

Yamada, Kohei

Kageyama, Akira

The Astrophysical Journal, 778:11 (14pp), 2013 November 20 doi:10.1088/0004-637X/778/1/11

EFFECTS OF PENETRATIVE CONVECTION ON SOLAR DYNAMO

Youhei Masada, Kohei Yamada, and Akira Kageyama
Department of Computational Science, Graduate School of System Informatics, Kobe University,
Kobe, Japan; ymasada@harbor.kobe-u.ac.jp
Received 2013 April 2; accepted 2013 September 10; published 2013 October 28

ABSTRACT

Spherical solar dynamo simulations are performed. A self-consistent, fully compressible magnetohydrodynamic system with a stably stratified layer below the convective envelope is numerically solved with a newly developed simulation code based on the Yin–Yang grid. The effects of penetrative convection are studied by comparing two models with and without the stable layer. The differential rotation profile in both models is reasonably solar-like with equatorial acceleration. When considering the penetrative convection, a tachocline-like shear layer is developed and maintained beneath the convection zone without assuming any forcing. While the turbulent magnetic field becomes predominant in the region where the convective motion is vigorous, mean-field components are preferentially organized in the region where the convective motion is less vigorous. Particularly in the stable layer, the strong, large-scale field with a dipole symmetry is spontaneously built up. The polarity reversal of the mean-field component takes place globally and synchronously throughout the system regardless of the presence of the stable layer. Our results suggest that the stably stratified layer is a key component for organizing the large-scale strong magnetic field, but is not essential for the polarity reversal.

Key words: convection – dynamo – magnetohydrodynamics (MHD) – Sun: interior

Online-only material: color figures

1. INTRODUCTION

A grand challenge in solar physics is a construction of self-consistent theory that explains the observed large-scale spatial structures of the fields and their dynamical change in time. Two basic large-scale structures that remain to be explained are the azimuthal average of the azimuthal flow, $\bar{v}_\phi$, and the azimuthal average of the azimuthal magnetic field, $\bar{B}_\phi$. The averaged velocity, $\bar{v}_\phi$, is characterized by the conical isorotation profile in the meridian plane and the thin tachocline layer with steep angular velocity gradient (e.g., Thompson et al. 2003). The averaged magnetic field, $\bar{B}_\phi$, is characterized by an antisymmetric profile with respect to the equator and the polarity reversals with the pseudo-periodicity of 22 yr (e.g., Hathaway 2010). See Ossendrijver (2003) and Miesch (2005, 2012) for reviews.

To reproduce the large-scale structures and dynamics, magnetohydrodynamic (MHD) simulations have been performed both in the global (spherical shell) geometry (e.g., Gilman & Miller 1981; Gilman 1983; Glatzmaier 1985) and in the local Cartesian geometry (e.g., Meneguzzi & Pouquet 1989; Cattaneo et al. 1991; Nordlund et al. 1992; Brandenburg et al. 1996).

The first modern solar dynamo simulation with solar values of luminosity, background stratification, and rotation rate was performed by Brun et al. (2004). They solved anelastic MHD convection system in the domain that extends over 0.72–0.97 $R_\odot$, spanning the bulk of the convection zone. While the solar-like equatorial acceleration and the dynamo-generated magnetic field with strengths of order 5000 G was achieved, the mean large-scale magnetic field was relatively weak and did not exhibit periodic polarity reversals.

Browning et al. (2006) showed, in an anelastic spherical shell dynamo simulation with the presence of the tachocline, that strong axisymmetric toroidal magnetic fields can be formed in the stably stratified layer below the convection zone. The associated mean poloidal magnetic fields showed the dipole dominance, but they did not exhibit polarity reversals. While the solar-like rotation profile was achieved in their simulations, a mechanical forcing was necessary to maintain the thin tachocline layer with steep angular velocity gradient.

Solar dynamo simulations that successfully produced the cyclic large-scale magnetic fields were presented in Ghizaru et al. (2010) and Racine et al. (2011). Their simulations are based on an anelastic model that is commonly used in the global circulation models of the Earth's atmosphere with a cooling term to force the system toward the ambient state (e.g., Prusa et al. 2008; Smolarkiewicz & Szmelter 2009). The solar-like thin tachocline layer was developed as a consequence of the cooling as well as the low dissipation embodied in their numerical scheme. They showed that the large-scale magnetic field is built up in the tachocline layer and exhibits polarity reversals when the temporal integration of the simulation was calculated long enough.

The large-scale dynamo activity was found not only in the anelastic models but also in the compressible dynamo simulation. Käpylä et al. (2010) performed the dynamo simulation with the penetrative convection in a spherical-wedge geometry (e.g., Brandenburg et al. 2007). Using a weakly stratified dynamo model, they succeeded in simulating the formation and the cyclic polarity reversal of the large-scale magnetic field. Unlike Browning et al. (2006) and Ghizaru et al. (2010), the large-scale dynamo operated in the convection zone in their model. Despite the presence of the underlying stable layer below the convective envelope, the spontaneous formation of the solar-like tachocline layer was not observed.

These numerical studies that targeted the solar dynamo have made it increasingly clear that the underlying stable layer below the convection zone is an important building block for the solar dynamo. It seems to play a crucial role in the formation of the solar-like $\bar{v}_\phi$ and $\bar{B}_\phi$. However, there is no research that directly compares two dynamo simulations differing only in the presence and absence of the underlying stable layer.

In Miesch et al. (2009), the influence of the tachocline on the magnetic dynamo was reviewed by comparing two previous simulations done by Brun et al. (2004) and Browning et al. (2006). While the two simulation models are both based on the same simulation code with solar values of the luminosity, rotation rate, and background stratification, they adopt different diffusivities and grid spacings that can affect the convective motion and magnetic dynamo. To get a better grasp of the role of the stably stratified layer in the solar dynamo mechanism, the influences of parameters other than the presence of the stable layer should be eliminated. This is one of the motivations of our study.

In this paper, we perform a fully compressible spherical solar dynamo simulation with a stably stratified layer below the convection zone. Formations of the key profiles of the solar interior, i.e., the solar-like $\bar{v}_\phi$ and $\bar{B}_\phi$, and the spontaneous polarity reversals are reproduced without assuming any forcing in the fundamental equations. To elucidate the effects of the penetrative convection, two simulations with and without the stable layer below the convection zone are compared.

Another purpose of this paper is to report a development of new program code for the solar dynamo simulation. A lot of simulation models for the global dynamo are spectral-based type, using the spherical harmonics expansion (e.g., Brun et al. 2004). The spherical harmonics expansion method is, however, believed to be confronted with the parallel scaling difficulty when tens of thousands or more processor cores are used. A different approach to massively parallel solar dynamo model is strongly required for the present peta- or coming exa-scale era. We have developed a global solar dynamo simulation code based on the grid point-based approach.

The spherical geometry imposes difficulties in the design of the spatial grid points to sustain high numerical efficiency, accuracy, and parallel scalability. We have proposed an overset grid method approach to the spherical geometry (Kageyama & Sato 2004). The grid system, Yin–Yang grid, is applied to geodynamo (e.g., Kageyama et al. 2008; Miyagoshi et al. 2010), mantle convection (e.g., Kameyama et al. 2008; Tackley 2008), supernova explosions (e.g., Müller et al. 2012; Lentz et al. 2012), and other astrophysical and geophysical simulations. The parallel scaling property of the spherical MHD simulation on the Yin–Yang grid is promising. It attained 46% (15.2 TFlops) of the peak performance of 4096 cores of the Earth Simulator supercomputer for the geodynamo simulations (Gordon Bell Award in Supercomputing 2004). Our new solar dynamo code is developed based on this Yin–Yang geodynamo code. This paper is our first report on the results obtained by this Yin–Yang solar dynamo code.

2. NUMERICAL SETTINGS

We numerically solve an MHD dynamo convection system in a spherical shell domain defined by $(0.6R \leqslant r \leqslant R)$, $(0 \leqslant \theta \leqslant \pi)$, and $(-\pi \leqslant \phi < \pi)$, where r, θ, and ϕ are the radius, colatitude, and longitude, respectively. Our model has two layers: upper convective layer of $0.3R$ thickness in the range of $(0.7R \leqslant r \leqslant R)$, and stably stratified lower layer of $0.1R$ thickness in $(0.6R \leqslant r \leqslant 0.7R)$.

The fundamental equations are the fully compressible MHD equations in the rotating frame of reference with a constant angular velocity, $\boldsymbol{\Omega} = \Omega_0 \boldsymbol{e}_z$, which is parallel to the coordinate axis ($\theta = 0$):

$$\frac{\partial \rho}{\partial t} = -\nabla \cdot \boldsymbol{f}, \tag{1}$$

$$\frac{\partial \boldsymbol{f}}{\partial t} = -\nabla \cdot (\boldsymbol{v}\boldsymbol{f}) - \nabla p + \boldsymbol{j} \times \boldsymbol{B} + \rho \boldsymbol{g} + 2\rho \boldsymbol{v} \times \boldsymbol{\Omega} + \mu \left[\nabla^2 \boldsymbol{v} + \frac{1}{3} \nabla (\nabla \cdot \boldsymbol{v}) \right], \tag{2}$$

$$\frac{\partial p}{\partial t} = -\boldsymbol{v} \cdot \nabla p - \gamma p \nabla \cdot \boldsymbol{v} + (\gamma - 1)[\nabla \cdot (\kappa \nabla T) + \eta \boldsymbol{j}^2 + \Phi], \tag{3}$$

$$\frac{\partial \boldsymbol{A}}{\partial t} = \boldsymbol{v} \times \boldsymbol{B} - \eta \boldsymbol{j}, \tag{4}$$

with

$$\Phi = 2\mu \left[e_{ij} e_{ij} - \frac{1}{3} (\nabla \cdot \boldsymbol{v}) \right], \quad e_{ij} = \frac{1}{2} \left(\frac{\partial v_i}{\partial x_j} + \frac{\partial v_j}{\partial x_i} \right),$$
$$\boldsymbol{g} = -g_0 / r^2 \boldsymbol{e}_r, \quad \boldsymbol{B} = \nabla \times \boldsymbol{A}, \quad \boldsymbol{j} = \nabla \times \boldsymbol{B}.$$

Here, the mass density, ρ, pressure, p, mass flux, $\boldsymbol{f} = \rho \boldsymbol{v}$, and the magnetic field's vector potential, $\boldsymbol{A}$, are the basic variables. We assume an ideal gas law $p = (\gamma - 1)\epsilon$ with $\gamma = 5/3$, where ϵ is the internal energy. The viscosity, electrical resistivity, and thermal conductivity are represented by μ, η, and κ, respectively.

The initial condition is a hydrostatic equilibrium which is described by a piecewise polytropic distribution with the polytropic index m (e.g., Käpylä et al. 2010),

$$\frac{dT}{dr} = \frac{g_0}{c_v(\gamma - 1)(m + 1)}. \tag{5}$$

We choose $m = 1$ and 3 for the upper convection layer and the lower stable layer, respectively. The thermal conductivity is determined by requiring a constant luminosity, L, defined by $L \equiv -4\pi\kappa r^2 dT/dr$, throughout the domain.

We solve the MHD equations in a non-dimensional form. Normalization quantities are defined by setting $R = g_0 = \rho_0 = 1$, where ρ_0 is the initial density at $r = 0.6R$. We normalize length, time, velocity, density, and magnetic field in units of R, $\sqrt{R^3/g_0}$, $\sqrt{g_0/R}$, ρ_0, and $\sqrt{g_0 \rho_0 / R}$. We define the Prandtl, magnetic Prandtl, and Rayleigh numbers by

$$\mathrm{Pr} = \frac{\mu}{\kappa}, \quad \mathrm{Pm} = \frac{\mu}{\eta}, \quad \mathrm{Ra} = \frac{GMd^4 \rho_m^2}{\mu\kappa R^2} \left(-\frac{\mathrm{d}s}{\mathrm{d}r} \right)_{r_m}, \tag{6}$$

where ρ_m is the density at the mid-convection zone ($r = r_m$), and $d = 0.3R$ is the depth of the convection zone. The stratification level is controlled by the normalized pressure scale height at the surface,

$$\xi_0 \equiv \frac{c_v(\gamma - 1)T_s}{g_0 R}, \tag{7}$$

where T_s is the temperature at $r = R$. In this work, we use $\xi_0 = 0.3$, yielding a small density contrast of about 3. Figure 1 shows the radial distributions of the initial temperature, density, and pressure adopted for our numerical model by solid,

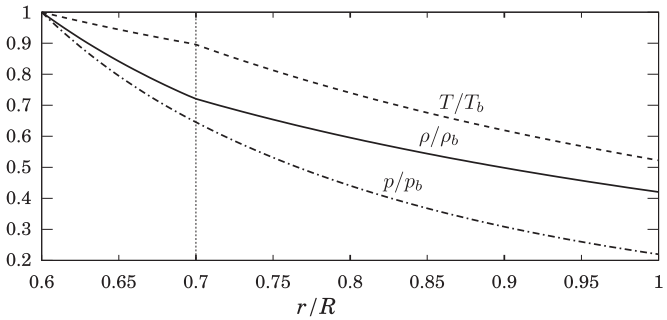

Figure 1. Radial profiles of the initial temperature (solid), initial density (dashed), and initial pressure (dash-dotted) adopted in our convective dynamo simulation. The vertical axis is normalized by their values at $r = 0.6R$.

dashed, and dash-dotted curves, respectively. The vertical axis is normalized by the value at $r = 0.6R$. The radial slopes in our numerical model are more gentle than the solar profiles. These give the convective motion with the Mach number of $\mathcal{O}(10^{-2})$.

The relative importance of rotation in the convection is measured by the Coriolis number

$$\mathrm{Co} = \frac{2\Omega_0 d}{v_{\mathrm{rms}}}, \tag{8}$$

where $v_{\mathrm{rms}} \equiv \langle\langle v_\theta^2 + v_r^2\rangle\rangle^{1/2}$ is the mean velocity. The double angular brackets denote the time and volume average in the convection zone in the saturated state. The convective turnover time and the equipartition strength of magnetic field are defined, respectively, by

$$\tau_c \equiv \frac{d}{v_{\mathrm{rms}}}, \quad B_{\mathrm{eq}} \equiv \langle\langle \rho\ (v_\theta^2 + v_r^2)\rangle\rangle^{1/2}. \tag{9}$$

The stress-free boundary condition for the velocity is imposed on the two spherical boundaries. We assume the perfect conductor boundary condition for the magnetic field ($A_r = A_\theta = A_\phi = 0$) on the inner surface, and the radial field condition ($A_r = 0, \partial A_\theta/\partial r = -A_\theta/r, \partial A_\phi/\partial r = -A_\phi/r$) on the outer surface. A constant energy flux is imposed on the inner boundary. The temperature is fixed to be T_s on the outer boundary.

The Equations (1)–(4) are discretized by the second-order central difference on the Yin–Yang grid. Each of the two congruent grids, the Yin grid and Yang grid, covers a partial spherical shell region defined as ($\pi/4 \leqslant \theta \leqslant 3\pi/4, -3\pi/4 \leqslant \phi \leqslant 3\pi/4$). They are combined in a complemental way to cover a whole spherical shell as shown in Figure 2. The regions surrounded by red and blue curves are assigned to the Yin and Yang grids, respectively. Physical quantities on the horizontal boarders of the Yin or Yang grids are set by mutual interpolations. For the time integration, the standard fourth-order Runge–Kutta method is used. Since the Yin–Yang grid is free from the coordinate singularity and the grid concentration around there, we can avoid the severe time-step constraint due to the CFL condition. See Kageyama & Sato (2004) for details on the Yin–Yang grid method. The computation is performed in parallel using MPI (Message Passing Interface).

Non-dimensional parameters $\mathrm{Pr} = 0.2$, $\mathrm{Pm} = 4.0$, and $\mathrm{Ra} = 1.2 \times 10^5$, and constant angular velocity of $\Omega_0 = 0.4$ are adopted in all the calculations reported here in order to achieve the Coriolis number expected in the convection zone of the Sun [$\mathrm{Co} \simeq \mathcal{O}(1)$]. The total grid size for the run with the upper convection layer and the lower stable layer (Model A)

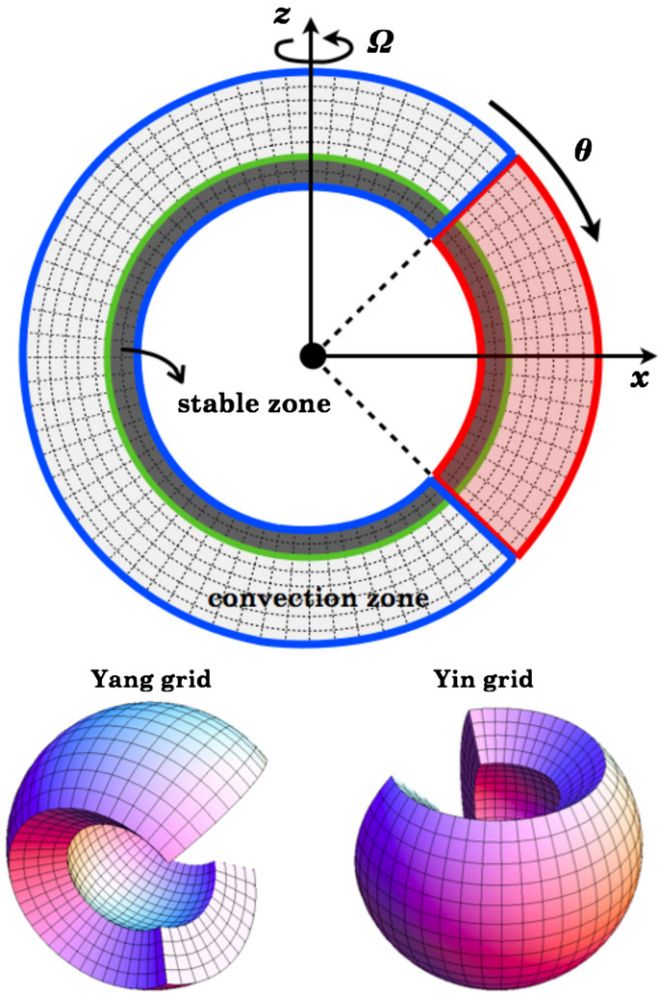

Figure 2. Calculation domain and Yin–Yang grid. Each of the two congruent grids, the Yin grid and Yang grid, cover a partial spherical shell region defined as ($\pi/4 \leqslant \theta \leqslant 3\pi/4, -3\pi/4 \leqslant \phi \leqslant 3\pi/4$). They are combined in a complemental way to cover a whole spherical shell. The domains surrounded by red and blue curves are assigned to the Yin and Yang grids, respectively.

(A color version of this figure is available in the online journal.)

is 121 (in r) $\times$402 (in θ) $\times$ 402 (in ϕ) $\times$2 (Yin & Yang). A model without the stable layer (Model B) is also studied, in the domain ($0.7R \leqslant r \leqslant R$), with the same physical parameters and the same grid spacings ($91 \times 402 \times 402 \times 2$). A random temperature perturbation and weak magnetic field are seeded in the convection zone when the calculation starts.

3. NUMERICAL RESULTS

Figure 3 shows the temporal evolution of the volume-averaged kinetic and magnetic energies defined by

$$\epsilon_{\mathrm{kin}} = \int \frac{1}{2}\rho \mathbf{v}^2 dV \Big/ \int dV, \quad \epsilon_{\mathrm{mag}} \equiv \int \frac{\mathbf{B}^2}{2\mu_0} \Big/ \int dV, \tag{10}$$

for Models A and B. The red and orange curves correspond to those for Model A. The blue and green curves are for Model B. After the convective motion sets in, it reaches a nonlinear saturation state at around $t = 30\tau_c$. The saturation levels of the convection kinetic energy for Models A and B are almost the same. The mean velocity is $v_{\mathrm{rms}} = 0.03$ which yields $B_{\mathrm{eq}} = 0.02$, $\mathrm{Co} = 8.0$, and $\tau_c = 10.0$ for both models. We have run the simulations up to $500\tau_c$ and then compared the

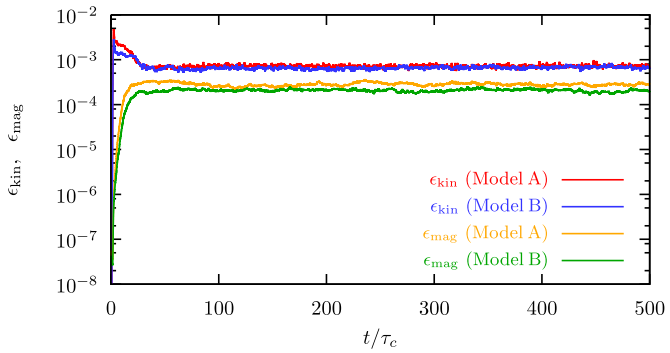

Figure 3. Temporal evolutions of volume-averaged kinetic and magnetic energies ($\epsilon_{\rm kin}$ and $\epsilon_{\rm mag}$) for Models A and B. The red and orange curves denote $\epsilon_{\rm kin}$ and $\epsilon_{\rm mag}$ for Model A, and the blue and green curves are those for Model B.

(A color version of this figure is available in the online journal.)

physical properties of convections, mean flows, and magnetic dynamos between the two models.

To examine the convective and magnetic structures in detail, we define the following four averages of a function $h(\theta, \phi)$ on a sphere.

The latitudinal average:

$$\langle h \rangle_\theta \equiv \frac{1}{2} \int_{-1}^{1} h(\theta, \phi)\, \mathrm{d}\cos\theta, \tag{11}$$

The longitudinal average:

$$\langle h \rangle_\phi \equiv \frac{1}{2\pi} \int_{-\pi}^{\pi} h(\theta, \phi)\, \mathrm{d}\phi, \tag{12}$$

The spherical average:

$$\langle h \rangle_s \equiv \frac{1}{4\pi} \int_{-1}^{1} \int_{-\pi}^{\pi} h(\theta, \phi)\, \mathrm{d}\cos\theta\, \mathrm{d}\phi, \tag{13}$$

The northern hemispheric average:

$$\langle h \rangle_+ \equiv \frac{1}{2\pi} \int_{0}^{1} \int_{-\pi}^{\pi} h(\theta, \phi)\, \mathrm{d}\cos\theta\, \mathrm{d}\phi. \tag{14}$$

The time-average of each spatial mean is denoted by additional angular brackets, such as $\langle\langle h \rangle_\theta\rangle$.

3.1. Properties of Convective Motion

Figure 4 shows, in the Mollweide projection, the distribution of the radial velocity when $t = 330\tau_c$ on spherical surfaces at different depths for two models. Panels (a)–(c) correspond to the depths $r = 0.95R$, $0.85R$, and $0.72R$ for Model A, and panels (d)–(f) are those for Model B. The orange and blue tones depict upflow and downflow velocities. At the upper ($r = 0.95R$) and mid- ($r = 0.85R$) convection zones, the convective motion is characterized by upflow dominant cells surrounded by networks of narrow downflow lanes for both models. The higher the latitude, the smaller the convective cell prevails. Elongated columnar convective cells aligned with the rotation axis appear near the equator. These are the typical features observed in rotating stratified convection (e.g., Spruit et al. 1990; Miesch et al. 2000; Brummell et al. 2002; Brun et al. 2004). In panel (c), we find that the downflow lanes persist in the plume-like coherent structure even just above the bottom of the unstable layer ($r = 0.72R$). The downflow plumes then penetrate into the underlying stable layer.

The radial profile of the mean radial velocity $\langle\langle v_r^2 \rangle_s\rangle^{1/2}$ is shown in Figure 5. The red solid and blue dashed curves correspond to Models A and B, respectively. The time average spans in the range of $300\tau_c \leqslant t \leqslant 400\tau_c$. The mean radial velocity has a peak at the mid-convection zone ($r \sim 0.8R$) for both models. The convective motion is the most active there. While the radial flow is restrained by the boundary placed on the bottom of the convection zone in Model B, it can penetrate into the underlying stable layer in Model A. As a result of the penetrative convection, mean zonal and meridional flows are driven by the Reynolds and Maxwell stresses in the stable layer. This will be described in the following sections.

3.2. Structures of Mean Flow

In Figures 6(a) and (b), time-averaged mean angular velocity, defined by $\langle\langle\Omega\rangle_\phi\rangle = \langle\langle v_\phi \rangle_\phi\rangle/(r\sin\theta) + \Omega_0$, is shown for models A and B, respectively. The time average spans in the range of

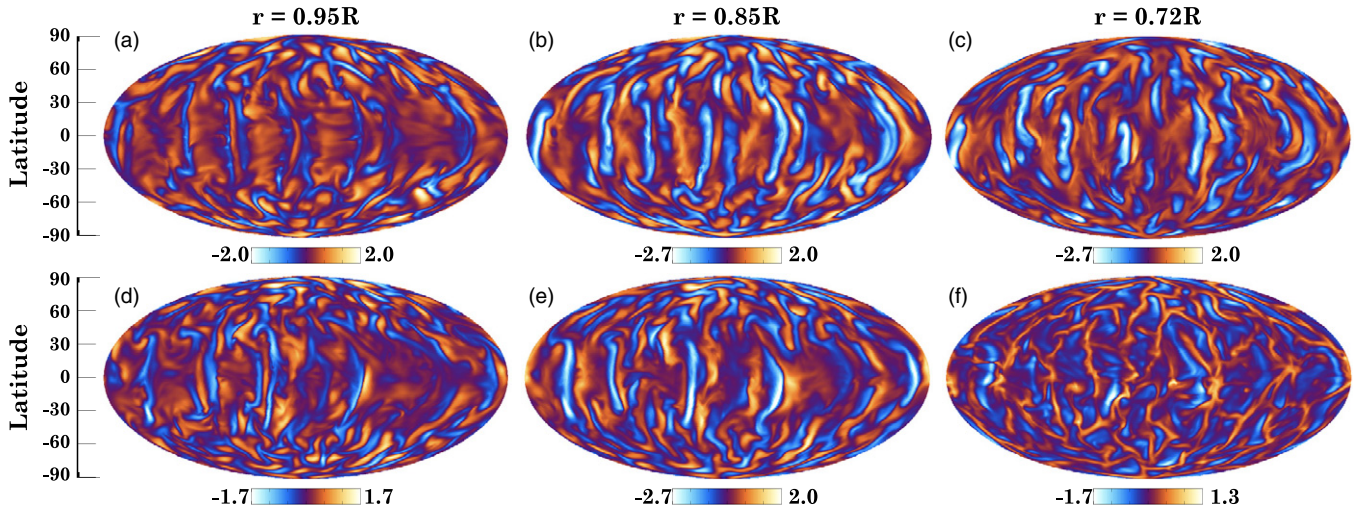

Figure 4. Distribution of radial velocity on spherical surfaces at sampled radii $v_r(\theta, \phi)$ when $t = 330\tau_c$ (in the Mollweide projection). Panels (a)–(c) correspond to the radii $r = 0.95R$, $0.85R$, and $0.72R$ for Model A, and panels (d)–(f) are those for Model B. The orange and blue tones depict upflow and downflow velocities normalized by $v_{\rm rms} = 0.03$.

(A color version of this figure is available in the online journal.)

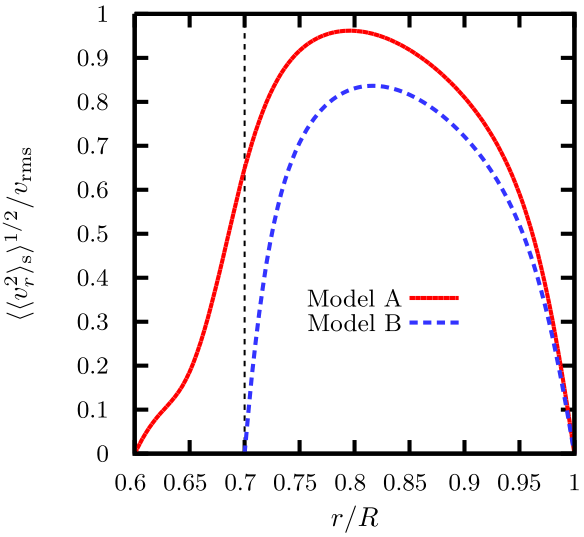

Figure 5. Radial profile of the mean radial velocity $\langle\langle v_r^2\rangle_s\rangle^{1/2}$. The time average spans in the range of $300\tau_c \leqslant t \leqslant 400\tau_c$. The vertical axis is normalized by $v_{\rm rms} = 0.03$. The red solid and blue dashed curves correspond to Models A and B, respectively. The vertical dashed line denotes the base of the convection zone.

(A color version of this figure is available in the online journal.)

$300\tau_c \leqslant t \leqslant 400\tau_c$. The normalization unit is the initial angular velocity, Ω_0.

The differential rotations in both models basically have solar-like profiles with the equatorial acceleration. However, both exhibit more cylindrical alignment than the solar rotation profile characterized by the conical isorotation surface. The system is dominated by the Taylor–Proudman balance in both models (e.g., Pedlosky 1987). The angular velocity contrast, $\Delta\Omega$, between equator and pole is about 18% in Model A and 16% in Model B. These are slightly smaller than that obtained by the helioseismology (∼20%). More remarkably, a radial gradient of the angular velocity is developed in the stably stratified layer around latitudes ±40°. This structure is reminiscent of the solar tachocline despite the fact that the radial shear layer is broad compared to the observed one (Spiegel & Zahn 1992; Charbonneau et al. 1999; Miesch 2005; Hughes et al. 2007). The rotation profile of Model A is reasonably similar with that of the Sun deduced from helioseismology (Thompson et al. 2003).

The spontaneous formation of the tachocline-like shear layer below the convective envelope was reported in the hydrodynamic simulation of the solar penetrative convection performed by Brun et al. (2011). Our results suggest that the tachocline-like shear layer is a natural outcome of the presence of the stable layer even in the MHD convection system. We discuss more about the differential rotation profile established in Model A in Section 4.1.

Figures 6(c) and (d) show the time-averaged mean meridional flows for the models A and B. The color contour depicts the meridional flow velocity, defined by $\langle\langle v_m\rangle_\phi\rangle = [\langle\langle v_r\rangle_\phi\rangle^2 + \langle\langle v_\theta\rangle_\phi\rangle^2]^{1/2}$, with a maximum $\sim 0.1 v_{\rm rms}$. The streaklines are overplotted with a length proportional to the flow speed. The circulation flow is primarily counter-clockwise in the bulk of the convection zone in the northern hemisphere, that is, the poleward in the upper convection zone and the equatorward in the bottom convection zone in both models. However, there is a clear difference in the circulation pattern between the two models. While a large single-cell is formed in Model B, Model A shows a double-cell pattern with a strong inward/outward flow at the low/mid-latitudes. An intriguing finding is that the equatorward component penetrates into the underlying stable layer when the radial gradient of the angular velocity resides

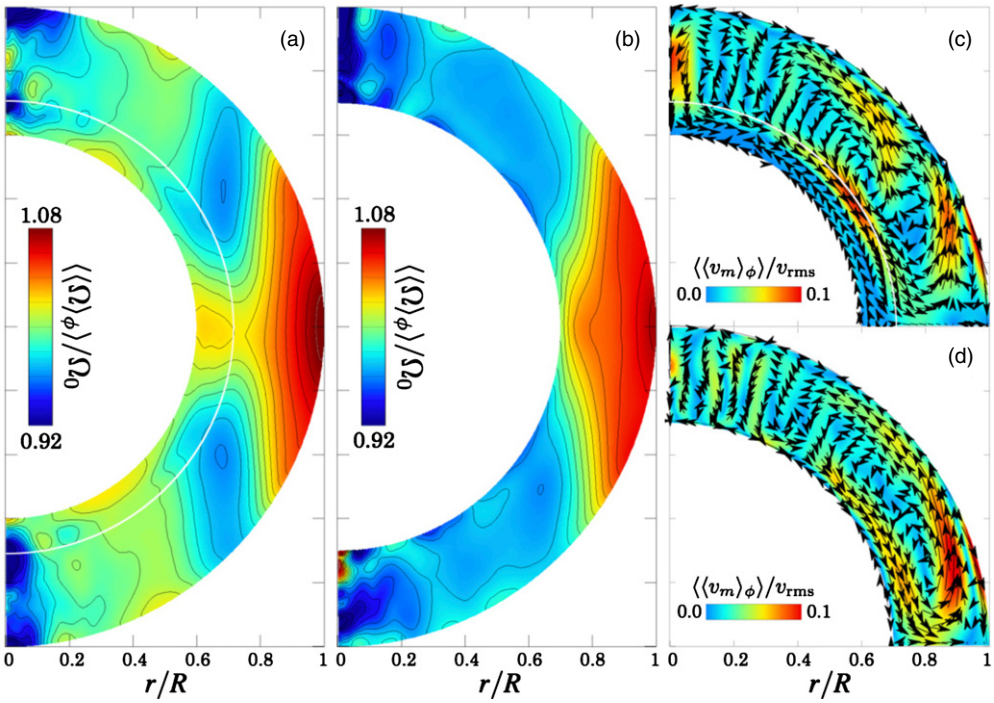

Figure 6. Mean angular velocity $\langle\langle\Omega\rangle_\phi\rangle$ (panels (a) and (b) for Models A and B), and mean meridional flow (panels (c) and (d) for Models A and B), where $\langle\langle\Omega\rangle_\phi\rangle = \langle\langle v_\phi\rangle_\phi\rangle/(r\sin\theta) + \Omega_0$. The mean meridional flow velocity is defined by $\langle\langle v_m\rangle_\phi\rangle = [\langle\langle v_r\rangle_\phi\rangle^2 + \langle\langle v_\theta\rangle_\phi\rangle^2]^{1/2}$. The white solid curves in panels (a) and (c) denote the interface between the convective and stable layers.

(A color version of this figure is available in the online journal.)

(see Figure 6(a)). This suggests that the penetrative transport of magnetic flux by the meridional flow might play a role in magnetic dynamo in our model.

The meridional flow takes a role in transporting angular momentum and magnetic flux in the Sun. However, the circulation pattern, velocity, and their time variations are still controversial as compared with the mean angular velocity profile which is well-confirmed by the helioseismic measurement. This is because the meridional circulation is much weaker than the differential rotation. Although the global circulation consisting of two cells is implied by the helioseismic inversion (see Mitra-Kraev & Thompson 2007) and is also obtained by numerical simulation (e.g., Miesch et al. 2006), it is not agreed upon in general (Hathaway 2012; Schad et al. 2012).

The mean-field theory of the angular momentum transport predicts a single-cell circulation (e.g., Ruediger 1989). Despite the fact that the kinematic flux-transport dynamo model is constructed based on the single-cell circulation (Dikpati & Charbonneau 1999; Charbonneau 2005), the influence of the circulation pattern on the magnetic activity is still a matter of debate (Pipin & Kosovichev 2013 and references therein). In order to accomplish more detailed discussion about the meridional flow, we should improve our simulation model in such a way to achieve smaller-scale subsurface convection ranging from granulation to super-granulation as probed by local helioseismology (Gizon & Birch 2005; Rieutord & Rincon 2010).

3.3. Structures of Magnetic Field

As shown in Figure 3, the magnetic energy is amplified by the dynamo action and is saturated at a level of about 40% of the convective kinetic energy for both models after $t \simeq 30\tau_c$. The magnetic field is maintained longer than the magnetic diffusion time ($\sim 100\tau_c$). Although the volume-averaged magnetic energy is almost the same in the models A and B, there are remarkable differences in the spatial structure of the magnetic fields.

The time and surface average of the magnetic energy density is presented as a function of radius in Figure 7. The broken solid lines with red squares, blue circles, and green diamonds denote the contributions from radial, latitudinal, and azimuthal components of the magnetic field for Model A, respectively. The broken dashed lines with the same symbols denote those for Model B. The time average spans in the range of $100\tau_c \leqslant t \leqslant 400\tau_c$. While the contributions of three magnetic components are almost the same at the mid-convection zone ($r \simeq 0.85$) where the convective motion is vigorous, the azimuthal component becomes predominant in the region where the convective motion is less active for both models (see also Figure 5). Particularly in the stable layer of Model A, most of the magnetic energy is stored as a form of the azimuthal field.

To examine the magnetic structure in more detail, we divide the magnetic energy density into an axi-symmetric part and an asymmetric part (see the Appendix)

$$\langle \boldsymbol{B}^2 \rangle_s = \langle \bar{B}_r^2 \rangle_\theta + \langle \bar{B}_\theta^2 \rangle_\theta + \langle \bar{B}_\phi^2 \rangle_\theta + (\text{asymmetric part}), \quad (15)$$

where we denote the axi-symmetric part of the magnetic field B_i for $i = r, \theta, \phi$,

$$\bar{B}_i \equiv \langle B_i \rangle_\phi. \quad (16)$$

To elucidate the relative strengths of axi-symmetric components, we plot the profiles of $\langle \langle \bar{B}_i^2 \rangle_\theta \rangle / \langle \langle B^2 \rangle_s \rangle$ in Figure 8(a). The broken solid lines with red squares, blue circles, and green diamonds denote the radial, latitudinal, and azimuthal components for Model A, respectively. The broken dashed lines with the same symbols denote those for Model B. The time average spans in the range of $100\tau_c \leqslant t \leqslant 400\tau_c$. Among the three axi-symmetric components, $\bar{B}_\phi$ is dominant. The tendency of $\bar{B}_\phi$–dominance is apparent not only in the stable layer, but also in the convection zone in both models A and B. The relative strength of the axi-symmetric component increases with the depth and reaches the maximum at around the bottom stable zone. Figures 7 and 8(a) suggest that the axi-symmetric component is built up in the convectively calm layer although the magnetic energy is amplified preferentially in the region where the vigorous convective motion exits.

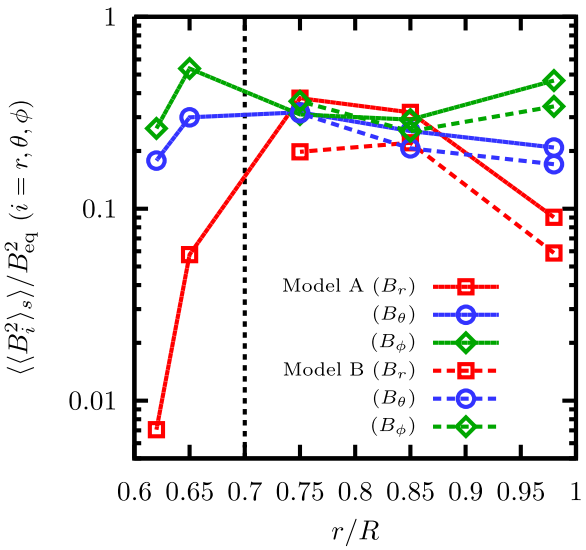

Figure 7. Time and surface average of the magnetic energy density as a function of radius. The sampled radii are $r/R = 0.62, 0.65, 0.75, 0.85, 0.98$ for Model A, and $r/R = 0.75, 0.85, 0.98$ for Model B. The broken solid lines with red squares, blue circles, and green diamonds denote the contributions from radial, latitudinal, and azimuthal components of the magnetic field for Model A. The broken dashed lines with the same symbols denote those for Model B. The time average spans in the range of $100\tau_c \leqslant t \leqslant 400\tau_c$. The vertical axis is normalized by the square of $B_{\rm eq}(= 0.02)$.

(A color version of this figure is available in the online journal.)

We then analyze the latitudinal moments of the axi-symmetric field, $\bar{\boldsymbol{B}}$. We focus on $\bar{B}_r$ since this component purely reflects the poloidal field, while $\bar{B}_\theta$ and $\bar{B}_\phi$ are a mixture of the toroidal and poloidal fields. From the Perseval's equation (see the Appendix),

$$\langle \bar{B}_r^2 \rangle_\theta = \frac{1}{2} \sum_{l=1} (\bar{B}_r)_l^2, \quad (17)$$

where

$$(\bar{B}_r)_l = \int_{-1}^{1} \bar{B}_r P_l^*(\cos\theta)\, \mathrm{d}\cos\theta. \quad (18)$$

Here P_l^* are normalized Legendre polynomials. Figure 8(b) shows profiles of $\langle (\bar{B}_r)_l^2 \rangle / 2 \langle \langle \bar{B}_r^2 \rangle_\theta \rangle$ for $l = 1, 2$, and 3. The broken solid lines with red squares, blue circles, and green diamonds denote dipole ($l = 1$), quadrupole ($l = 2$), and octupole ($l = 3$), moments for Model A, respectively. The broken dashed lines with the same symbols denote those for Model B. The time average spans in the range of $100\tau_c \leqslant t \leqslant 400\tau_c$. There is not much difference among amplitudes of dipole, quadrupole, and octupole moments at all depths. Nevertheless, it would be worth noting that Model B has a octupole dominance in almost the whole domain. In the case of Model A, the dipole gradually becomes dominant with the depth. It is predominant

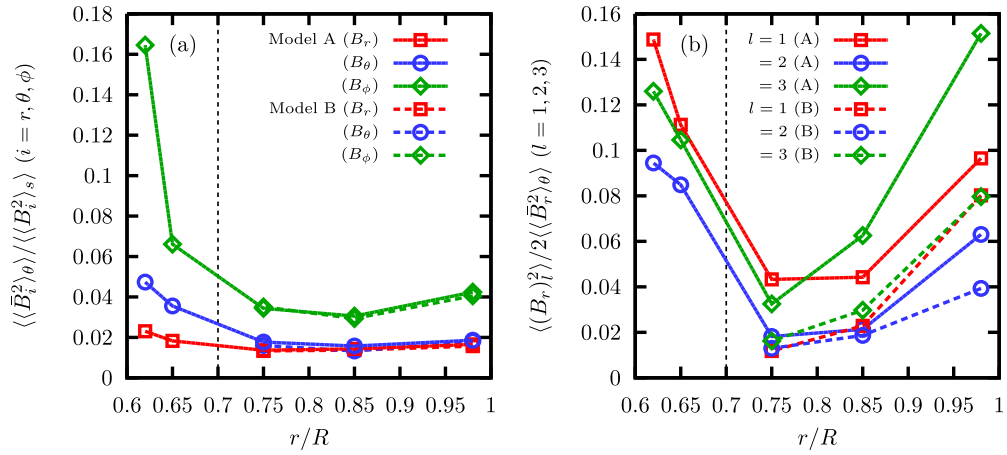

Figure 8. (a) Profiles of $\langle\langle\bar{B}_i^2\rangle_\theta\rangle/\langle\langle B^2\rangle_s\rangle$ for $i = r, \theta, \phi$. (b) Profiles of $\langle(\bar{B}_r)_l^2\rangle/2\langle\langle\bar{B}_r^2\rangle_\theta\rangle$ for $l = 1$, 2, and 3. The broken solid lines with red squares, blue circles, and green diamonds denote the radial, latitudinal, and azimuthal components in panel (a), dipole ($l = 1$), quadrupole ($l = 2$), and octupole ($l = 3$) moments in panel (b) for Model A. The broken dashed lines with the same symbols denote those for Model B. The time average spans in the range of $100\tau_c \leqslant t \leqslant 400\tau_c$.

(A color version of this figure is available in the online journal.)

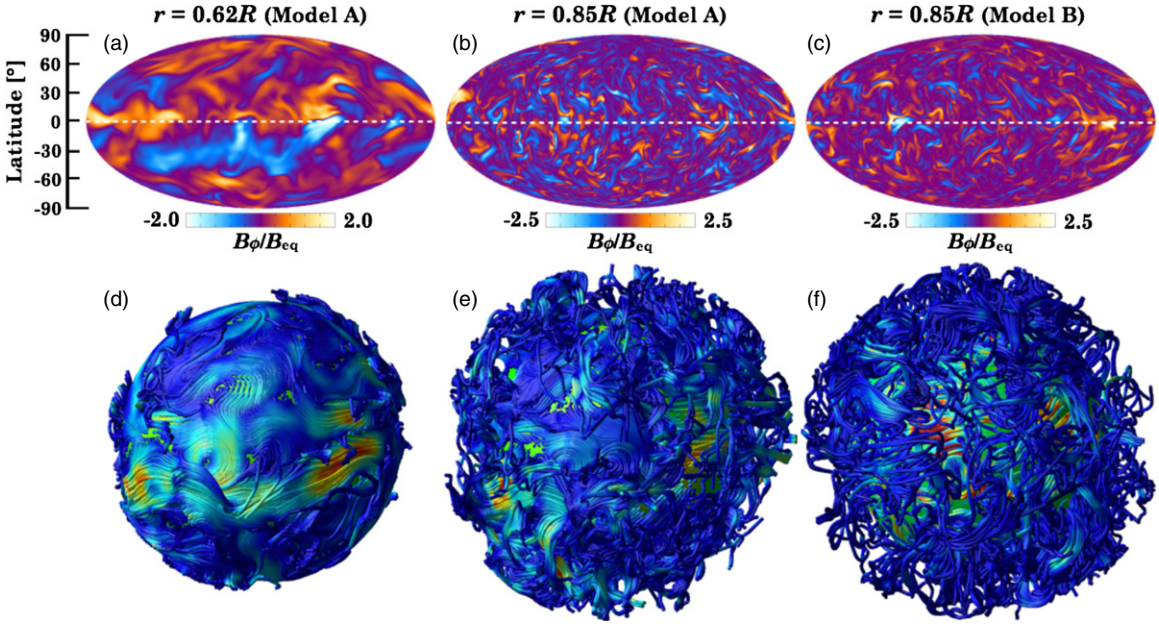

Figure 9. Snapshot of the azimuthal component of the magnetic field B_ϕ when $t = 330\tau_c$ on a spherical surface at sampled radii (a) $r = 0.62R$ and (b) $r = 0.85R$ for Model A, and (c) $r = 0.85R$ for Model B. The orange and blue tones depict positive and negative values of the B_ϕ component. The magnetic field lines at the time and position corresponding to those in panels (a)–(c) are visualized in panels (d)–(f), respectively.

(A color version of this figure is available in the online journal.)

in the bottom convection zone and the stable zone although the upper and mid-convection zones are dominated by higher multipoles like in Model B. The stably stratified layer below the convective envelope promotes the dipole solution as indicated by Miesch et al. (2009).

The similarity and differences of the magnetic structure between two models are the most obvious on the azimuthal component of the magnetic field. A snapshot of the azimuthal component of the magnetic field at $t = 330\tau_c$ is presented in Figure 9 on a spherical surface at (a) $r = 0.65R$ and (b) $r = 0.85R$ for Model A, and (c) $r = 0.85R$ for Model B. The orange and blue tones depict positive and negative values of the B_ϕ component normalized by $B_{\rm eq}$. The magnetic field lines at the time corresponding to those in the panels (a)–(c) are visualized in Figures 9(d)–(f), respectively. As expected from Figures 7 and 8, the convective envelope is dominated by disordered tangled magnetic field lines with a myriad of localized small-scale structures in both models. These incoherent magnetic fields are strongly influenced by vigorous convective motions and thus are highly intermittent. The horizontal converging flows sweep magnetic fields into downflow lanes and intensify them locally to the super-equipartition strength as was observed in existing convective dynamo simulations (e.g., Brandenburg et al. 1996; Cattaneo et al. 2003; Brun et al. 2004).

In the underlying stable layer of Model A, a strong large-scale azimuthal component of magnetic field is built up around the equator, and resides there for long time intervals. This well-organized magnetic component is roughly antisymmetric around the equatorial plane and has a maximum strength of an order of $B_{\rm eq}$. The large-scale component is organized in the stable zone where the radial angular velocity gradient resides (see Figure 6(a)). This would be important evidence of a connection

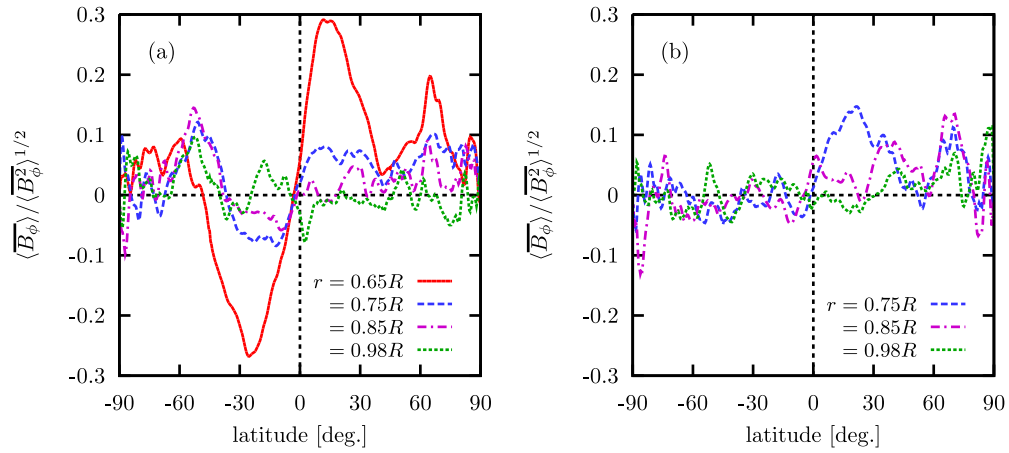

Figure 10. Latitudinal profiles of $\langle \bar{B}_\phi \rangle / \langle \overline{B_\phi^2} \rangle^{1/2}$ at the sampled radii for Models A and B. The red solid, blue dashed, purple dash-dotted, and green dotted curves correspond to $r = 0.65R$, $0.75R$, $0.85R$, and $0.98R$, respectively. The time average spans in the range of $240\tau_c \leqslant t \leqslant 340\tau_c$ for Model A or $310\tau_c \leqslant t \leqslant 360\tau_c$ for Model B.

(A color version of this figure is available in the online journal.)

between the deep-seated, large-scale magnetic component and the tachocline-like shear layer that is spontaneously developed in the model with the stable layer.

The latitudinal profiles of $\langle \bar{B}_\phi \rangle / \langle \overline{B_\phi^2} \rangle^{1/2}$ are shown at the sampled radii in Figures 10(a) and (b) for Models A and B. The red solid, blue dashed, purple dash-dotted, and green dotted curves correspond to $r = 0.65R$, $0.75R$, $0.85R$, and $0.98R$, respectively. The time average spans in the range of $240\tau_c \leqslant t \leqslant 340\tau_c$ for Model A or $310\tau_c \leqslant t \leqslant 360\tau_c$ for Model B. As shown in Figures 8(a) and 9, the strong mean azimuthal component with the antisymmetric profile is built up around the equatorial plane in the stable layer of Model A. It reaches maximum strength around the latitude $\pm 25^\circ$. While the antisymmetric property of the mean-field is found not only in the stable layer but also in the convective envelope, the amplitude of the mean-field component is much smaller in the convection zone than in the stable zone. In comparison with Model A, the antisymmetric property of the mean azimuthal field is weaker in Model B.

Overall, magnetic structures simulated in our models indicate that the stably stratified layer is an important building block to organize large-scale magnetic components and supports the numerical studies of Browning et al. (2006) and Ghizaru et al. (2010). Despite the magnetic energy being amplified by the vigorous convective motion in the mid-convection zone, the strong mean magnetic component is preferentially organized in the region where the convective motion is less vigorous. This suggests that the downward pumping process of the magnetic flux is of great importance in the solar dynamo mechanism (Tobias et al. 2001, 2008; Barker et al. 2012). The implementation of more realistic convective penetration and downward pumping processes into the numerical modeling might be the first to reproduce the solar dynamo.

3.4. Cyclic Property of Magnetic Fields

One of the most interesting findings in our simulation is that the large-scale magnetic fields show polarity reversals. Figure 11 gives an azimuthally averaged magnetic field as a function of time and latitude for Model A. Panels (a), (b), and (c) represent $\bar{B}_r$, $\bar{B}_\theta$, and $\bar{B}_\phi$ at $r = 0.65R$. The large-scale $\bar{B}_\phi$ with antisymmetric parity persists over a relatively long period despite strong stochastic disturbances due to penetrative convective motions. The $\bar{B}_\phi$ component changes sign for at least three times, at about $t = 100\tau_c$, $t = 210\tau_c$, and $t = 350\tau_c$ (panel (c)).

As for the poloidal component of the magnetic field, it shows the dipole dominance in the stable layer as indicated in Figure 8(b). During 30–$100\tau_c$ when a strong $\bar{B}_\phi$ component with positive polarity dominates in the northern hemisphere, negative $\bar{B}_r$ and positive $\bar{B}_\theta$ are observed (panels (a) and (b)). While the $\bar{B}_\theta$ component has the same sign in both of the hemispheres, the $\bar{B}_r$ component has opposite polarity in the two hemispheres. When the $\bar{B}_\phi$ reversal takes place, the other two components $\bar{B}_r$ and $\bar{B}_\theta$ also change sign. See, for example, at about $t = 100\tau_c$ in Figure 11.

The time-latitude diagram of an azimuthally averaged magnetic field for Model B is shown in Figure 12. Panels (a), (b), and (c) represent $\bar{B}_r$, $\bar{B}_\theta$, and $\bar{B}_\phi$ at $r = 0.75R$. The mean-field component shows a weak polarity preference and polarity reversals in time even in the model without the stable layer. While the $\bar{B}_\phi$ component has an antisymmetric profile with respect to the equator, the $\bar{B}_\theta$ component has the same sign in both the hemispheres as does Model A. However, the amplitude, coherency, and dipole dominance of the mean magnetic component are much weaker in model B compared with those in the model A. These are consistent with Figures 8–10.

As indicators of the depth-dependency of the polarity reversal, we show the temporal evolution of the dipole moment $(\bar{B}_r)_{l=1}$ defined by Equation (18) and the northern hemispheric average of the azimuthal field $\langle B_\phi \rangle_+$ in Figure 13. Panels (a) and (b) correspond to $(\bar{B}_r)_{l=1}$ and $\langle B_\phi \rangle_+$ for Model A. Panels (c) and (d) are those for Model B. The red, blue, and green curves correspond to the depths $r = 0.65R$, $0.75R$, and $0.85R$, respectively. The polarity reversal takes place not only in the underlying stable layer but also in the convective envelope for Model A. It is remarkable that there is a clear phase synchronization in the polarity reversals at different depths. Even in the case of Mode B, the polarity reversal of the mean-field component is noticeable although the short-term variability is superimposed onto the global long-term modulation. The cycle period is about $100\tau_c$ for both models. This indicates that the polarity reversal of the mean-field component is a

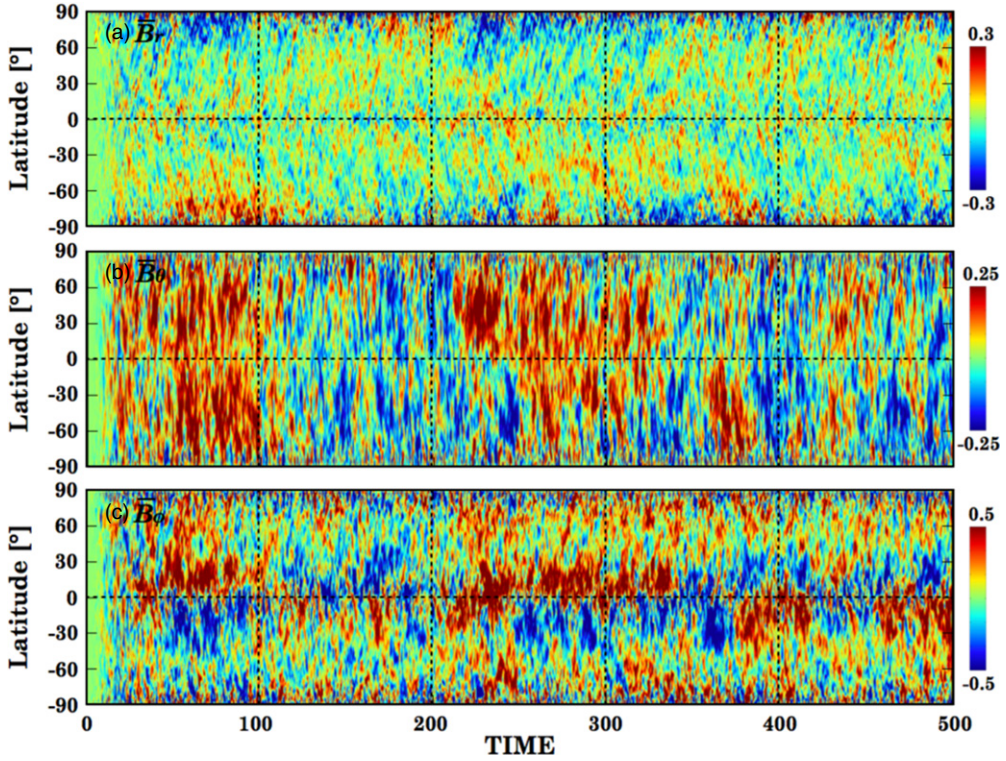

Figure 11. Azimuthally averaged magnetic field as a function of time and latitude for Model A. The top, middle, and bottom panels correspond to $\bar{B}_r$, $\bar{B}_\theta$, and $\bar{B}_\phi$ at the depth $r = 0.65R$. The red and blue tones depict positive and negative values of each magnetic component.
(A color version of this figure is available in the online journal.)

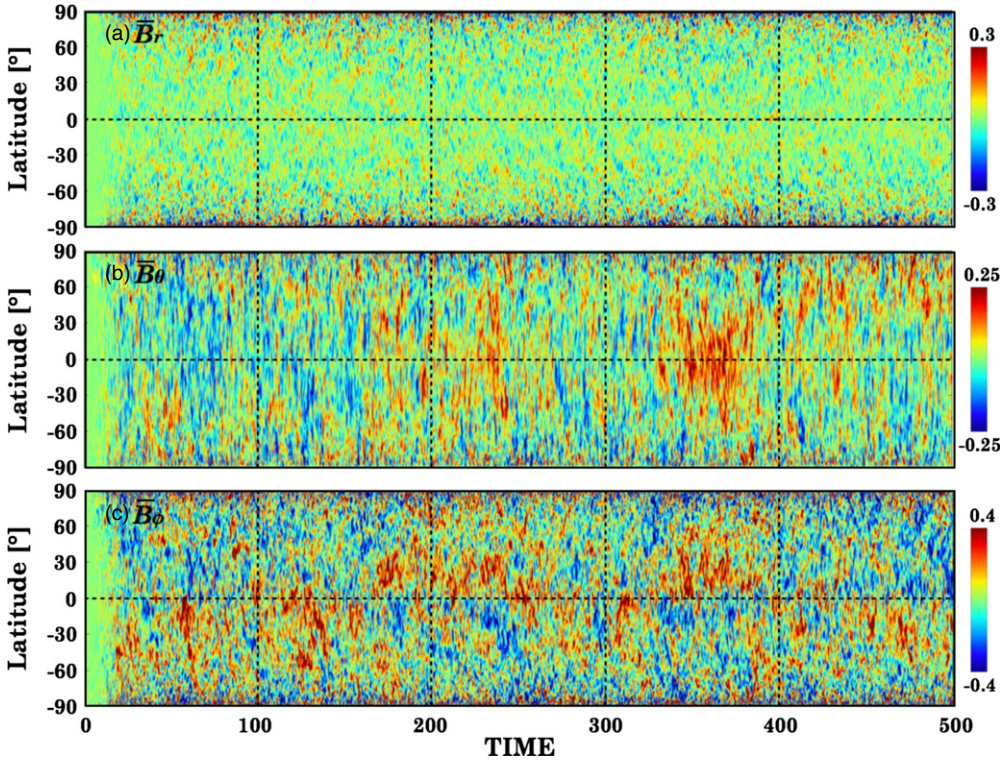

Figure 12. Azimuthally averaged magnetic field as a function of time and latitude for Model B. The top, middle, and bottom panels correspond to $\bar{B}_r$, $\bar{B}_\theta$, and $\bar{B}_\phi$ at the depth $r = 0.72R$. The red and blue tones depict positive and negative values of each magnetic component.
(A color version of this figure is available in the online journal.)

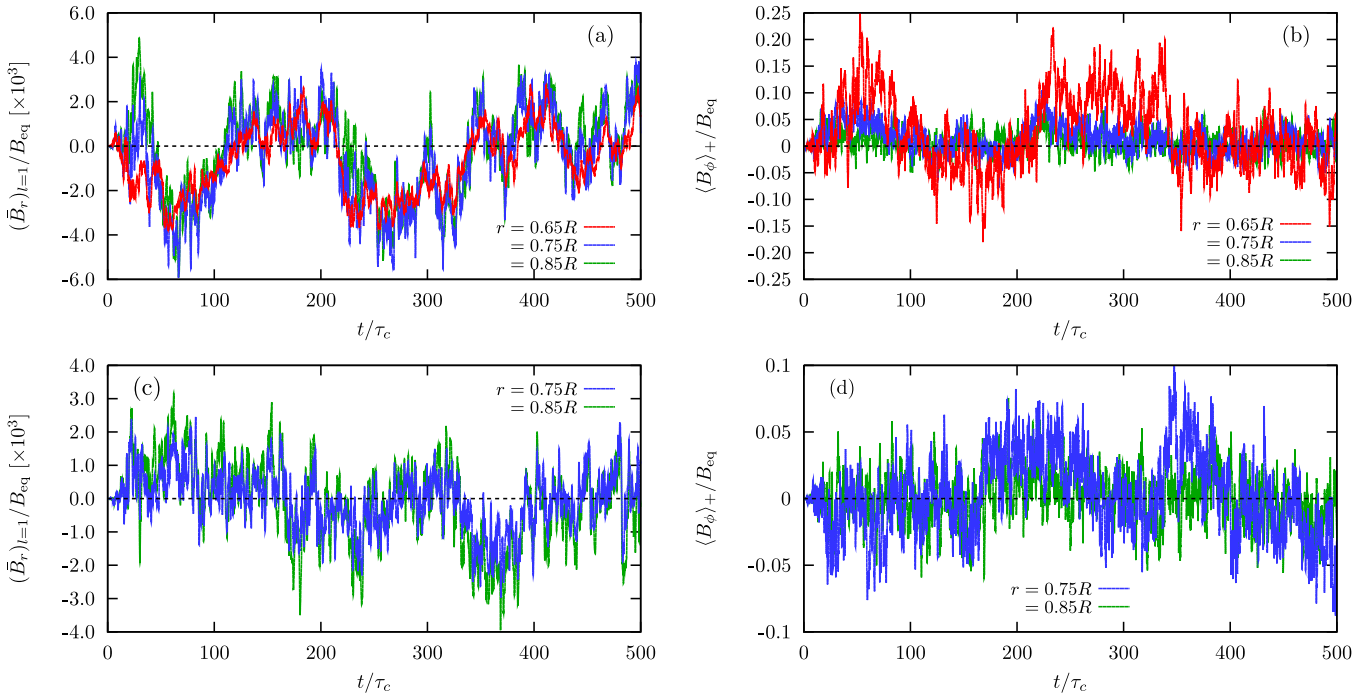

Figure 13. Temporal evolutions of (a) the dipole moment $(\bar{B}_r)_{l=1}$ and (b) the northern hemispheric average of the azimuthal field $\langle B_\phi \rangle_+$. Panels (a) and (b) correspond to $(\bar{B}_r)_{l=1}$ and $\langle B_\phi \rangle_+$ for Model A. Panels (c) and (d) are those for Model B. The red, blue, and green curves correspond to the depths $r = 0.65R$, $0.75R$, and $0.85R$, respectively.

(A color version of this figure is available in the online journal.)

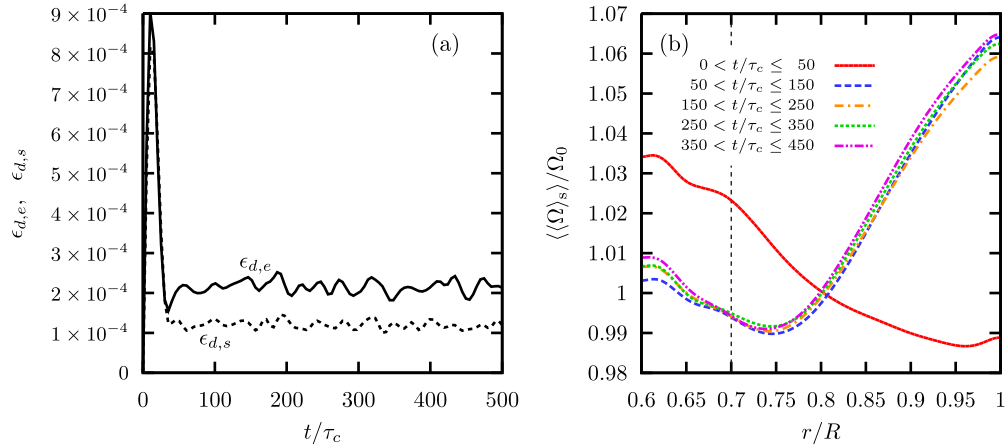

Figure 14. (a) Temporal evolution of the kinetic energy of differential rotation averaged over the entire volume ($\equiv \epsilon_{d,e}$) and over the radiative zone ($\equiv \epsilon_{d,s}$). (b) Radial profile of the mean angular velocity averaged over a given time span $\langle\langle\Omega\rangle_s\rangle$ for Model A. The different line types correspond to different time spans. Note that the surface average here is taken over the range of $60^\circ \leqslant \theta \leqslant 120^\circ$ (around the equator).

(A color version of this figure is available in the online journal.)

global phenomenon that takes place synchronously throughout the system regardless of the presence of the stable layer.

4. DISCUSSION

4.1. Force Balance in Differential Rotation

The helioseismic measurements suggest that the tachocline thickness is less than 4% of the solar radius (e.g., Elliott & Gough 1999; Charbonneau et al. 1999; Basu & Antia 2001). The presence of such a thin transition layer leads to the tachocline confinement problem (Spiegel & Zahn 1992). The mechanism that inhibits the differential rotation in the convection zone to spread into the deeper radiative interior is still an open problem, though several theoretical models have been proposed (Ruediger & Kitchatinov 1997; Gough & McIntyre 1998; Rogers 2011; Brun et al. 2011).

In conjunction with the tachocline confinement problem, we examine the time evolution of the differential rotation established in our simulation model with the stably stratified layer (Model A). We show, in Figure 14(a), the temporal evolution of the kinetic energy of differential rotation averaged over the entire volume ($\equiv \epsilon_{d,e}$) and the volume of the stable zone ($\equiv \epsilon_{d,s}$) defined by

$$\epsilon_{d,e} = \int_{r \leqslant 1.0R} \left[\frac{1}{2} \rho v_\phi^2 \right] dV \Big/ \int_{r \leqslant 1.0R} dV,$$

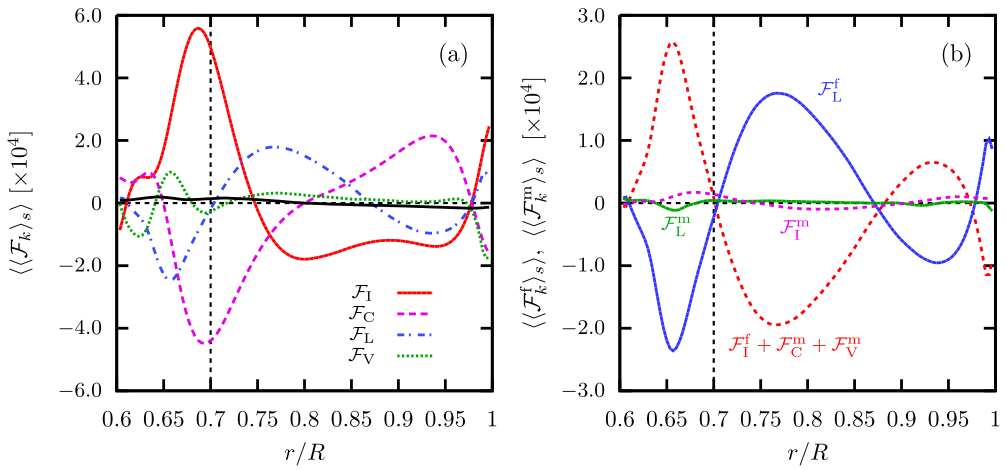

Figure 15. (a) Time and surface averages of various force terms as function of radius. The solid red, dashed magenta, dash-dotted blue, and dotted green curves correspond to the radial profiles of the inertia, Coriolis, Lorentz, and viscous forces, respectively. The solid black curve denotes the sum of the four azimuthal forces. (b) The radial profiles of $\langle\langle\mathcal{F}_{\rm I}^{\rm f}\rangle_s\rangle + \langle\langle\mathcal{F}_{\rm C}^{\rm m}\rangle_s\rangle + \langle\langle\mathcal{F}_{\rm V}^{\rm m}\rangle_s\rangle$ and $\langle\langle\mathcal{F}_{\rm I}^{\rm m}\rangle_s\rangle$ by the red-dashed and magenta dashed curves. The blue and green solid curves denote the radial profiles of $\langle\langle\mathcal{F}_{\rm L}^{\rm f}\rangle_s\rangle$ and $\langle\langle\mathcal{F}_{\rm L}^{\rm m}\rangle_s\rangle$.

(A color version of this figure is available in the online journal.)

$$\epsilon_{d,s} = \int_{r\leqslant 0.7R}\left[\frac{1}{2}\rho v_\phi^2\right]dV \Big/ \int_{r\leqslant 0.7R} dV. \qquad (19)$$

After the initial transitional stage $t \lesssim 50\tau_c$, the kinetic energy of the differential rotation is settled into an approximately constant value both in the entire domain and in the stable zone. In our simulation, the viscous spreading of the tachocline-like shear layer operates on a timescale of $\tau_{\rm vis} \sim 50\tau_c$. This dominates over the radiative spreading controlled by the Eddington-Sweet timescale. Since the duration of the simulation is about $10\tau_{\rm vis}$, the differential rotation has achieved the equilibrated profile.

The statistical stationarity of the differential rotation profile is confirmed in Figure 14(b), which shows the radial profile of the mean angular velocity averaged over a given time span, $\langle\langle\Omega\rangle_{\rm s}\rangle$, for Model A. The different lines correspond to different time spans. Here the surface average is taken over the range of $60^\circ \leqslant \theta \leqslant 120^\circ$ (around the equator). After the initial evolutionary stage ($t \lesssim 50\tau_c$), the differential rotation attains a stationary profile in which the outer shell is rotating faster. The differential rotation in the convection zone does not spread downward into the stable layer as time passes in spite of the shear on the interface of the convection and stable layers.

The formation of the solar-like rotation profile is associated with the development of the magnetic field. As seen in the mean rotation profile during $0 \leqslant t \lesssim 50\tau_c$, the inner shell rotates faster than the outer shell at the early dynamo kinematic stage. When the magnetic field is sufficiently amplified, it begins to affect the convective motion. The rotation profile changes to the opposite state in which the outer shell is rotating faster. This implies that the dynamo-generated magnetic field plays an important role in establishing the solar-like differential rotation.

To elucidate the azimuthal force balance maintaining the differential rotation, we will consider the azimuthal component of momentum equation. The right-hand side of the equation is divided into four force terms:

$$\begin{aligned}
\mathcal{F}_{\rm I}(\rho, \boldsymbol{v}, \boldsymbol{B}) &\equiv [-{\rm div}(\rho\boldsymbol{v}\boldsymbol{v})]_\phi,\\
\mathcal{F}_{\rm C}(\rho, \boldsymbol{v}, \boldsymbol{B}) &\equiv [2\rho\boldsymbol{v}\times\boldsymbol{\Omega}]_\phi,\\
\mathcal{F}_{\rm L}(\rho, \boldsymbol{v}, \boldsymbol{B}) &\equiv [(\nabla\times\boldsymbol{B})\times\boldsymbol{B}]_\phi,\\
\mathcal{F}_{\rm V}(\rho, \boldsymbol{v}, \boldsymbol{B}) &\equiv [\mu(\nabla^2\boldsymbol{v} + \nabla(\nabla\cdot\boldsymbol{v})/3)]_\phi, \qquad (20)
\end{aligned}$$

where $\mathcal{F}_{\rm I}$ is the inertia force, $\mathcal{F}_{\rm C}$ is the Coriolis force, $\mathcal{F}_{\rm L}$ is the Lorentz force, and $\mathcal{F}_{\rm V}$ is the viscous force. Note that azimuthal pressure gradient force does not contribute to the mean azimuthal force balance. These four force terms should cancel out each other for retaining the statistical equilibrium.

The time and surface average of the each force term is demonstrated as a function of radius in Figure 15(a). The solid red, dashed magenta, dash-dotted blue, and dotted green curves correspond to the radial profiles of the inertia, Coriolis, Lorentz, and viscous forces, respectively. The solid black curve denotes the sum of the four azimuthal forces. The time average is taken over $280\tau_c \leqslant t \leqslant 300\tau_c$ with 200 snapshot data. The azimuthal force balance is mainly dominated by the inertia, Coriolis, and Lorentz forces. In the convection zone, the negative inertia force balances with the sum of the positive Coriolis and Lorentz forces. In contrast to that, the positive inertia force is compensated by the sum of the negative Coriolis and Lorentz forces in the stable zone. The positive peak of $\mathcal{F}_{\rm I}$ below the interface between the convection zone and stable zone indicates the angular momentum transport by the penetrative convection. The viscous force makes a minor contribution to the azimuthal force balance except for the surface layer and the bottom of the stable zone. The net azimuthal force represented by the solid black curve is nearly zero, confirming the statistical equilibrium of the azimuthal flow not only in the convection zone, but also in the stable zone.

To examine the azimuthal force balance in more detail, we divide each force term into the contributions of the axisymmetric mean components given by $\mathcal{F}_k^{\rm m} = \mathcal{F}_k(\bar\rho, \bar{\boldsymbol{v}}, \bar{\boldsymbol{B}})(k = {\rm I, C, L, V})$ and the contributions of the fluctuation components by $\mathcal{F}_k^{\rm f} = \mathcal{F}_k - \mathcal{F}_k^{\rm m}$. Figure 15(b) illustrates the roles of the mean and fluctuation components in the azimuthal force balance. Here we show the radial profiles of $\langle\langle\mathcal{F}_{\rm I}^{\rm f}\rangle_s\rangle + \langle\langle\mathcal{F}_{\rm C}^{\rm m}\rangle_s\rangle + \langle\langle\mathcal{F}_{\rm V}^{\rm m}\rangle_s\rangle$ and $\langle\langle\mathcal{F}_{\rm I}^{\rm m}\rangle_s\rangle$ by the red dashed and magenta dashed curves, which are all flow origins. The blue and green solid curves denote the radial profiles of $\langle\langle\mathcal{F}_{\rm L}^{\rm f}\rangle_s\rangle$ and $\langle\langle\mathcal{F}_{\rm L}^{\rm m}\rangle_s\rangle$, which are magnetic field origins. The contributions of fluctuation components to Coriolis and viscous forces are negligibly small.

In the region where the convective motion is less vigorous (upper convection zone and stable zone), the positive azimuthal force due to the flow field is balanced with the negative force

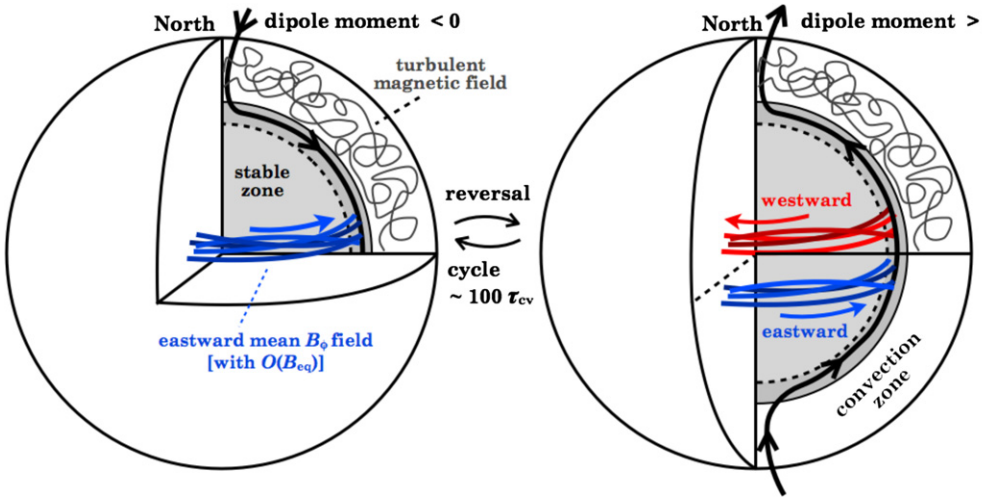

Figure 16. Schematic picture of the magnetic structure in the model with the stable layer. The thick black curve demonstrates the poloidal magnetic field. The blue and red curves denote the eastward and westward azimuthal magnetic components. The axi-symmetric large-scale azimuthal field with $\mathcal{O}(B_{\rm eq})(\simeq 10^4\ G)$ is preferentially organized around the equatorial region in the stably stratified layer, whereas the convection zone is dominated by the turbulent fluctuating magnetic component. The dipole dominance is one of remarkable features of the large-scale magnetic field rooted in the stable layer. The polarity reversal with the cycle period of $\sim 100\tau_c$ takes place globally and synchronously throughout the system.

(A color version of this figure is available in the online journal.)

sustained by the dynamo-generated magnetic field. In contrast, the negative azimuthal force due to the flow field is compensated by the positive Lorentz force in the most of the convection zone where the convective motion is vigorous. The Lorentz force by the nonlinear coupling of fluctuating magnetic field plays a crucial role in the azimuthal force balance for maintaining the equilibrated profile of the differential rotation.

As shown in Figure 6, the differential rotation profile established in our model exhibits more cylindrical alignment than the solar rotation profile characterized by the conical isorotation surface. Our MHD convection system is still dominated by the Taylor–Proudman balance. It is well known that the latitudinal entropy variation at the base of the convection zone induces a baroclinicity, and yields the solar-like conical rotation profile (e.g., Kitchatinov & Ruediger 1995; Rempel 2005; Miesch et al. 2006; Masada 2011). It might be important to numerically capture with higher accuracy the nonlinear MHD processes, such as instabilities and resultant turbulence in the stable layer to more accurately reproduce the large-scale solar convection profile.

4.2. Qualitative Picture of Magnetic Dynamo

Since the main purpose of this paper is not to accurately model the solar dynamo, but rather to reveal the effects of the penetrative convection on the magnetic dynamo process, the effective luminosity used in the simulation is larger than the solar value. Nevertheless, it would be helpful to evaluate the cycle period and the mean-field strength obtained in our simulation in comparing our model with the models of other groups.

Figures 13 gives the cycle period of the polarity reversal $\tau_{\rm cycle} \simeq 100\tau_c$, which is evaluated as

$$\tau_{\rm cycle} \simeq 100 \times \frac{d}{v_{\rm rms}} = 6.3\ \ [\rm yr], \tag{21}$$

when we adopt the solar values $d = 0.3\,R_\odot$ and $v_{\rm rms} \simeq 100\ \rm m\ s^{-1}$. This is about half of the cycle of the polarity reversal in the Sun. At the cycle maxima, the strength of the axi-symmetric azimuthal field in the stable zone reaches $B_{\rm eq}$, which can be evaluated as

$$B_{\phi,\rm max} = \left(4\pi\rho_m\ v_{\rm rms}^2\right)^{1/2} \simeq 8000\ \ [\rm G], \tag{22}$$

with the density $\rho_m \simeq 0.05\ \rm g\ cm^{-3}$ at the mid-convection zone of the Sun. This is a comparable strength with the large-scale magnetic field simulated in Browning et al. (2006) and Ghizaru et al. (2010), but would be an order of magnitude smaller than that expected in the tachocline layer of the Sun for explaining the sunspot emergence at the surface on latitudes of less than $\pm 40^\circ$ (e.g., Choudhuri & Gilman 1987).

When the numerical results are taken all together, the structure and evolution of the dynamo-generated magnetic field in our model is represented by a schematic picture in Figure 16. The thick black line demonstrates the poloidal magnetic component with dipole dominance. The blue and red curves denote eastward and westward azimuthal components. The mean large-scale azimuthal field with $\mathcal{O}(B_{\rm eq})$ is preferentially organized around the equatorial region in the stably stratified layer, whereas the convection zone is dominated by the turbulent fluctuating component. The polarity reversal with the cycle period of $\sim 100\tau_c$ takes place globally and synchronously throughout the system.

The dipole dominance is one of the remarkable features of the large-scale magnetic field rooted in the stable layer. The tendency of the dipole dominance that appears when taking account of the stable layer is reported in Browning et al. (2006) and Miesch et al. (2009). The differential rotation cannot only amplify the mean toroidal fields through the so-called Ω-effect, but can also expel the asymmetric field components via rotational smoothing process (Räedler 1986; Spruit 1999). The dipole-like magnetic structure with a large-scale axi-symmetric azimuthal component would thus be a natural outcome of the rotational amplification and smoothing of the magnetic field in the stable layer. The more accurate modeling of the stably stratified tachocline would enable us to tackle the generation mechanism of the large-scale $\mathcal{O}(10^5)$ G field that could be responsible for the origin of the sunspot on the solar surface.

We finally remark that both the equatorward migration and buoyant emergence of the large-scale magnetic component, that can bridge the gap between the simulation and sunspot observation, could not be simulated in our model. This clearly tells us that we still have a lot of missing components in order to effectively reproduce the solar interior in our dynamo modeling.

5. SUMMARY

We reported, in this paper, our initial results of solar dynamo simulation based on the Yin–Yang grid with the fully compressible MHD model. To investigate influences of the stably stratified layer below the convection zone, two simulation models with and without the stable layer (Models A and B) were compared. It is confirmed from our numerical study that the stable layer has a substantial influence on the convection and the magnetic field. Our main findings are summarized as follows.

1. The convective motion in the upper convection zone is characterized by upflow dominant cells surrounded by networks of narrow downflow lanes for both models. While the radial flow is restrained by the boundary placed on the bottom of the convection zone in Model B, the downflow lanes persist in the plume-like coherent structure even just above the bottom of the unstable layer in Model A. The downflow plumes then penetrate into the underlying stable layer.
2. The differential rotation profiles in both models are reasonably solar-like with equatorial acceleration. However, both exhibit more cylindrical alignment than the solar rotation profile with the conical isorotation surface inferred from the helioseismology. It is remarkable that the radial shear layer, which is reminiscent of the solar tachocline, is spontaneously developed without any forcing just beneath the convection zone as a result of the penetrative convection in Model A. The Lorentz force by the nonlinear coupling of the fluctuating magnetic field plays an important role in the azimuthal force balance for maintaining the solar-like differential rotation.
3. While the turbulent magnetic field becomes predominant in the region where the convective motion is vigorous, the mean-field component is preferentially built up in the region where the convective motion is less vigorous. Particularly in the stably stratified layer, the strong large-scale azimuthal component with antisymmetric profile with respect to the equator and the poloidal field with dipole dominance are spontaneously organized.
4. The mean magnetic component undergoes polarity reversals with the cycle period of $\sim 100\tau_c$ for both models. It takes place globally and synchronously throughout the system regardless of the presence of the stable layer. However, the amplitude, coherency, and dipole dominance of the mean magnetic component are much weaker in Model B compared with those in Model A. The stably stratified layer is a key component for organizing the large-scale strong magnetic field, but is not essential for the polarity reversal.

All the dynamo simulations reported here have used a relatively weak stratification with a density contrast of about 3 (see Section 2). The strong stratification in the actual Sun may have an influence on the physical properties of convections, mean flows, and magnetic dynamo (Käpylä et al. 2012, 2013). It is interesting that the three key features, solar-like $\bar{v}_\phi$, $\bar{B}_\phi$, and the polarity reversals are self-consistently reproduced, without assuming any forcing, even in the modest density stratification. Higher resolution simulations with a more realistic density stratification will facilitate our understanding of the physics of the solar convection and the solar dynamo. This is the next step with the Yin–Yang solar dynamo simulation code.

We thank the anonymous referee for constructive comments. Numerical computations were carried out on the π-Computer at Kobe Univ., the K-Computer at RIKEN, and the Cray XT4 at the National Astronomical Observatory of Japan. This work was supported by JSPS KAKENHI grant Nos. 24740125 and 20260052, and also by the Takahashi Industrial and Economic Research Foundation.

APPENDIX

DIVIDING SPHERICAL MEAN OF ENERGY INTO AXI-SYMMETRIC AND ASYMMETRIC PARTS

The purpose of this section is to split the spherical mean of energy into an axi-symmetric part and an asymmetric part. For a smooth function $h(\theta, \phi)$ on a sphere, we define the following three means:

Longitudinal mean:

$$\bar{h}(\theta) = \langle h(\theta, \phi)\rangle_\phi := \frac{1}{2\pi}\int_{-\pi}^{\pi} h(\theta, \phi)\,\mathrm{d}\phi, \tag{A1}$$

Latitudinal mean:

$$\langle h(\theta, \phi)\rangle_\theta := \frac{1}{2}\int_{-1}^{1} h(\theta, \phi)\,\mathrm{d}\cos\theta, \tag{A2}$$

Surface mean:

$$\begin{aligned}\langle h(\theta, \phi)\rangle_S :&= \frac{1}{4\pi}\int_{-1}^{1}\int_{-\pi}^{\pi} h(\theta, \phi)\,\mathrm{d}\cos\theta\,\mathrm{d}\phi \\ &= \langle\langle h\rangle_\phi\rangle_\theta = \langle\langle h\rangle_\theta\rangle_\phi.\end{aligned} \tag{A3}$$

We can always divide $h(\theta, \phi)$ into axi-symmetric and asymmetric parts:

$$h(\theta, \phi) = \bar{h}(\theta) + h_a(\theta, \phi). \tag{A4}$$

Note that

$$\langle h_a(\theta, \phi)\rangle_\phi = 0, \quad \langle\bar{h}(\theta)\rangle_S = \langle\bar{h}(\theta)\rangle_\theta. \tag{A5}$$

The surface mean of h^2 is also divided into two parts:

$$\langle h(\theta, \phi)^2\rangle_S = \langle(\bar{h} + h_a)^2\rangle_S \tag{A6}$$

$$= \langle(\bar{h})^2\rangle_S + 2\langle\bar{h}h_a\rangle_S + \langle(h_a)^2\rangle_S \tag{A7}$$

$$= \langle(\bar{h})^2\rangle_\theta + \langle(h_a)^2\rangle_S \quad \text{(cf. Equation (A5))}. \tag{A8}$$

Expanding $\bar{h}(\theta)$ by the normalized Legendre polynomials

$$P_\ell^*(\cos\theta) = \sqrt{\frac{2\ell+1}{2}}P_\ell(\cos\theta), \tag{A9}$$

that satisfy

$$\int_{-1}^{1} P_\ell^*\,P_{\ell'}^*\,\mathrm{d}\cos\theta = \delta_{\ell\ell'}, \tag{A10}$$

as

$$\bar{h}(\theta) = \sum_{\ell=0}^{\infty} H_\ell \, P_\ell^*(\cos\theta), \tag{A11}$$

we get the Perseval's equation,

$$\langle(\bar{h})^2\rangle_\theta = \frac{1}{2}\sum_{\ell=0}^{\infty} H_\ell^2, \tag{A12}$$

where Legendre coefficients H_ℓ are given by

$$H_\ell = \int_{-1}^{1} \bar{h}(\theta) \, P_\ell^*(\cos\theta)\, \mathrm{d}\cos\theta. \tag{A13}$$

Similarly, for a vector field $\boldsymbol{b}(\theta,\phi) = (b_r(\theta,\phi), b_\theta(\theta,\phi), b_\phi(\theta,\phi))$, we get

$$\langle \boldsymbol{b}^2\rangle_S = \sum_{i=\{r,\theta,\phi\}} \langle(b_i)^2\rangle_S \tag{A14}$$

$$= \sum_{i=\{r,\theta,\phi\}} \left[\langle(\bar{b}_i)^2\rangle_\theta + \langle(b_{i,a})^2\rangle_S\right], \tag{A15}$$

$$= \text{s.p.} + \text{a.p.} \tag{A16}$$

where the symmetric part

$$\text{s.p.} = \langle(\bar{b}_r)^2\rangle_\theta + \langle(\bar{b}_\theta)^2\rangle_\theta + \langle(\bar{b}_\phi)^2\rangle_\theta, \tag{A17}$$

and asymmetric part

$$\text{a.p.} = \sum_{i=\{r,\theta,\phi\}} \langle(b_{i,a})^2\rangle_S. \tag{A18}$$

Due to the Perseval's equation (A12), each of the three terms in Equation (A17) can be expanded as,

$$\langle(\bar{b}_i)^2\rangle_\theta = \frac{1}{2}\sum_{\ell=0}^{\infty}(\bar{B}_{i,\ell})^2 \tag{A19}$$

where $\bar{B}_{i,\ell}$ are Legendre coefficients

$$\bar{B}_{i,\ell} = \int_{-1}^{1} \bar{b}_i(\theta) \, P_\ell^*(\cos\theta)\, d\cos\theta. \tag{A20}$$

Note that for a magnetic field, the monopole component $\bar{B}_{r,\ell=0}$ is absent.

REFERENCES

Barker, A. J., Silvers, L. J., Proctor, M. R. E., & Weiss, N. O. 2012, MNRAS, 424, 115
Basu, S., & Antia, H. M. 2001, MNRAS, 324, 498
Brandenburg, A., Jennings, R. L., Nordlund, Å., et al. 1996, JFM, 306, 325
Brandenburg, A., Käpylä, P. J., Mitra, D., Moss, D., & Tavakol, R. 2007, AN, 328, 1118
Browning, M. K., Miesch, M. S., Brun, A. S., & Toomre, J. 2006, ApJL, 648, L157
Brummell, N. H., Clune, T. L., & Toomre, J. 2002, ApJ, 570, 825
Brun, A. S., Miesch, M. S., & Toomre, J. 2004, ApJ, 614, 1073
Brun, A. S., Miesch, M. S., & Toomre, J. 2011, ApJ, 742, 79
Cattaneo, F., Brummell, N. H., Toomre, J., Malagoli, A., & Hurlburt, N. E. 1991, ApJ, 370, 282
Cattaneo, F., Emonet, T., & Weiss, N. 2003, ApJ, 588, 1183
Charbonneau, P. 2005, LRSP, 2, 2
Charbonneau, P., Christensen-Dalsgaard, J., Henning, R., et al. 1999, ApJ, 527, 445
Choudhuri, A. R., & Gilman, P. A. 1987, ApJ, 316, 788
Dikpati, M., & Charbonneau, P. 1999, ApJ, 518, 508
Elliott, J. R., & Gough, D. O. 1999, ApJ, 516, 475
Ghizaru, M., Charbonneau, P., & Smolarkiewicz, P. K. 2010, ApJL, 715, L133
Gilman, P. A. 1983, ApJS, 53, 243
Gilman, P. A., & Miller, J. 1981, ApJS, 46, 211
Gizon, L., & Birch, A. C. 2005, LRSP, 2, 6
Glatzmaier, G. A. 1985, ApJ, 291, 300
Gough, D. O., & McIntyre, M. E. 1998, Natur, 394, 755
Hathaway, D. H. 2010, LRSP, 7, 1
Hathaway, D. H. 2012, ApJ, 760, 84
Hughes, D. W., Rosner, R., & Weiss, N. O. (ed.) 2007, The Solar Tachocline (Cambridge: Cambridge Univ. Press)
Kageyama, A., Miyagoshi, T., & Sato, T. 2008, Natur, 454, 1106
Kageyama, A., & Sato, T. 2004, GGG, 5, 9005
Kameyama, M., Kageyama, A., & Sato, T. 2008, PEPI, 171, 19
Käpylä, P. J., Korpi, M. J., Brandenburg, A., Mitra, D., & Tavakol, R. 2010, AN, 331, 73
Käpylä, P. J., Mantere, M. J., & Brandenburg, A. 2012, ApJL, 755, L22
Käpylä, P. J., Mantere, M. J., Cole, E., Warnecke, J., & Brandenburg, A. 2013, arXiv:1301.2595
Kitchatinov, L. L., & Ruediger, G. 1995, A&A, 299, 446
Lentz, E. J., Bruenn, S. W., Harris, J. A., et al. 2012, Proc. 12th Symp. on Nuclei in the Cosmos. PoS(NIC XII), 208
Masada, Y. 2011, MNRAS, 411, L26
Meneguzzi, M., & Pouquet, A. 1989, JFM, 205, 297
Miesch, M. S. 2005, LRSP, 2, 1
Miesch, M. S. 2012, RSPTA, 370, 3049
Miesch, M. S., Browning, M. K., Brun, A. S., Toomre, J., & Brown, B. P. 2009, in ASP Conf. Ser. 416, Solar-Stellar Dynamos as Revealed by Helio- and Asteroseismology: GONG 2008/SOHO 21, ed. M. Dikpati, T. Arentoft, I. González Hernández, C. Lindsey, & F. Hill (San Francisco, CA: ASP), 443
Miesch, M. S., Brun, A. S., & Toomre, J. 2006, ApJ, 641, 618
Miesch, M. S., Elliott, J. R., Toomre, J., et al. 2000, ApJ, 532, 593
Mitra-Kraev, U., & Thompson, M. J. 2007, AN, 328, 1009
Miyagoshi, T., Kageyama, A., & Sato, T. 2010, Natur, 463, 793
Müller, E., Janka, H.-T., & Wongwathanarat, A. 2012, A&A, 537, A63
Nordlund, A., Brandenburg, A., Jennings, R. L., et al. 1992, ApJ, 392, 647
Ossendrijver, M. 2003, A&ARv, 11, 287
Pedlosky, J. 1987, Geophysical Fluid Dynamics (New York: Springer)
Pipin, V. V., & Kosovichev, A. G. 2013, ApJ, 776, 36
Prusa, J.M., Smolarkiewicz, K., & Wyszogrodzki, A. 2008, CF, 37, 9
Racine, É., Charbonneau, P., Ghizaru, M., Bouchat, A., & Smolarkiewicz, P. K. 2011, ApJ, 735, 46
Räedler, K.-H. 1986, in Plasma Astrophysics, ESA Special Publication Vol. 251, ed. T. D. Guyenne & L. M. Zeleny (Noordwijk: ESA), 569
Rempel, M. 2005, ApJ, 622, 1320
Rieutord, M., & Rincon, F. 2010, LRSP, 7, 2
Rogers, T. M. 2011, ApJ, 733, 12
Ruediger, G., & Kitchatinov, L. L. 1997, AN, 318, 273
Ruediger, G. 1989, Differential Rotation and Stellar Convection. Sun and the Solar Stars (Berlin: Akademie)
Schad, A., Timmer, J., & Roth, M. 2012, AN, 333, 991
Smolarkiewicz, P. K., & Szmelter, J. 2009, JCoPh, 228, 33
Spiegel, E. A., & Zahn, J. P. 1992, A&A, 265, 106
Spruit, H. C. 1999, A&A, 349, 189
Spruit, H. C., Nordlund, A., & Title, A. M. 1990, ARA&A, 28, 263
Tackley, P. J. 2008, PEPI, 171, 7
Thompson, M. J., Christensen-Dalsgaard, J., Miesch, M. S., & Toomre, J. 2003, ARA&A, 41, 599
Tobias, S. M., Brummell, N. H., Clune, T. L., & Toomre, J. 2001, ApJ, 549, 1183
Tobias, S. M., Cattaneo, F., & Brummell, N. H. 2008, ApJ, 685, 596